Tilted, Extended, and Lying in Wait: The Membrane-Bound Topology of Residues Lys-381−Ser-405 of the Colicin E1 Channel Domain[†]

Zhikui Wei,[‡] Dawn White,[‡] Jie Wang,[§] Abdiwahab A. Musse,[‡] and A. Rod Merrill*,[‡]

Department of Molecular and Cellular Biology, University of Guelph, Guelph, ON, Canada N1G 2W1, and Department of Biochemistry and Cell Biology, State University of New York, Stony Brook, New York 11794-5215

Received February 14, 2007; Revised Manuscript Received March 22, 2007

ABSTRACT: The membrane-bound closed state (zero potential) of the helix 3 segment (Lys-381−Ser-405) of the colicin E1 channel domain was investigated by site-directed fluorescence labeling using a bimane probe tethered to a single cysteine residue of each mutant protein. A number of fluorescence properties of the tethered bimane probe were measured for the soluble channel mutant proteins as well as for the membrane-bound proteins. A new method called helical periodicity surface analysis was employed to fit the fluorescence data to a harmonic wave function using four different statistical methods. The fit of the various data sets to a harmonic wave function indicated that the periodicity of helix 3 in the membrane-bound state is typical for an amphipathic α helix (3.7−4.0 residues per turn and an angular frequency between 90 and 97°). Notably, upon membrane binding, helix 3 elongates from 15 residues (soluble structure) to 20 residues by a three- and two-residue extension at the N- and C-termini of the helix, respectively. Dual quencher analysis also revealed that helix 3 is appressed to the surface of the membrane with its N-terminus more deeply buried within the interfacial region of the bilayer than its C-terminus. Finally, contrary to a previous report, our data show that helices 3 and 4 remain separate and independent helices upon membrane association in the absence of a membrane potential.

Colicins are toxic proteins produced by bacteria of colicinogenic strains of *Escherichia coli* and some related species of Enterobacteriaceae during the growth of their cultures. Colicins are produced by these bacteria in response to a host of metabolic challenges, including DNA damage, anaerobiosis, catabolite repression, and nutrient depletion (*1*). Colicin E1 is a member of this large bacteriocin family of plasmid-encoded antimicrobial protein toxins secreted by *E. coli* in their struggles to survive in a hostile environment. These "killer proteins" target susceptible *E. coli* and similar bacteria, which do not possess the protective immunity protein (*2*), by acting at a number of levels, including (i) membrane depolarization via the formation of ion-conducting channels (*3*), (ii) inhibition of protein (*4*) or peptidoglycan synthesis (*5*), and (iii) DNA degradation (*6*). Due to their ability to invade related Gram-negative bacteria, colicins have become a model for studying bacterial protein import (*7*) as well as protein unfolding and folding (*8*, *9*), membrane insertion (*10*, *11*), and pore formation (*12*).

Colicin E1 belongs to the channel-forming group of colicins, which also includes colicins A, B, Ia, Ib, N, and K (*13*, *14*). The three-dimensional structures of these pore-forming colicins reveal that they consist of three domains: receptor binding, translocation, and catalytic domains. The receptor binding domain initiates entry of the toxin into the target cells (*15*) by binding with the BtuB or vitamin B_{12} receptor on the bacterial outer membrane (*16*, *17*). Next, the translocation domain associates with the trimeric β barrel TolC outer membrane receptor, through which the unfolded translocation and channel domains of the colicin are transported into the periplasm of the target bacterium (*17*). The channel domain subsequently adopts an insertion-competent conformation; the protein directly binds the inner membrane (*18*) and, in a series of kinetically defined steps, the channel protein sequentially unfolds, binds, and spontaneously inserts into the membrane in a precursor state to the open channel (*8*, *19*−*21*). The channel opens upon imposition of a trans-negative membrane potential (*22*), and the newly created pore causes depolarization of the cytoplasmic membrane through the escape of cellular ions such as Na^+, K^+, and H^+ and cell death ensues.

A crystal structure of the soluble channel domain of colicin E1 was determined to a resolution of 2.5 Å (*23*). The data revealed a globular protein comprised of 10 α helices similar to the structure of colicin A (*24*). Subsequently, the whole or channel domain structures of pore-forming colicins Ia (*25*), N (*26*), and B (*27*) have been determined, and predictably, they are all structurally similar. These structures suggest that a key to their pore forming ability is two distinct hydrophobic helices that create a membrane-spanning hairpin upon bilayer association (*19*, *28*, *29*). Interestingly, this feature of the colicin structure is also seen in the mammalian intracellular apoptotic regulators Bcl-2 (*30*), Bcl-$_{XL}$ (*31*), Bax (*32*), and

---

[†] This work was supported by a grant from the Natural Sciences and Engineering Research Council of Canada (to A.R.M.).

* To whom correspondence should be addressed: Department of Molecular and Cellular Biology, University of Guelph, Guelph, ON, Canada N1G 2W1. Telephone: (519) 824-4120, ext. 53806. Fax: (519) 837-1802. E-mail: rmerrill@uoguelph.ca.

[‡] University of Guelph.

[§] State University of New York.

10.1021/bi700317k CCC: $37.00

Bid (*33*), proteins known to create pores upon association with the mitochondrial or endoplasmic reticulum membranes.

A host of techniques and approaches have been employed over the years to derive information about the membrane-associated closed channel topology of the channel domain of colicin E1. Solid-state NMR methods were used to identify the transmembrane and in-plane α helices of membrane-bound colicin E1 (*20*), while circular dichroism, Fourier transform infrared spectroscopy, FRET, and differential scanning calorimetry were used to study membrane association and determine the α helical and β sheet content (*34*). Using site-directed mutagenesis to design the colicin E1 channel peptide with Trp residues, our group has mapped the location of the helical segments within the channel domain upon binding to the membrane using fluorescence quenching, FRET, hydrophobic mismatch, and red-edge excitation shift analysis (*29*, *35*−*37*). These diverse studies imply that hydrophobic helices 8 and 9 insert into the bacterial cytoplasmic membrane, while the associated amphipathic helices are splayed out upon the membrane surface with considerable interaction with the aqueous medium. The exact orientation of the helices, their depth of bilayer penetration, and the lipid and protein contacts made by each residue upon membrane binding are currently under investigation. Using electron paramagnetic resonance, the mobility and accessibility of nitroxide-labeled cysteine side chains generated one at a time from residues 402−424 (which encompass helix 4) showed a solvent-exposed and a lipid-exposed face of the amphipathic helix, suggesting a possible transmembrane orientation of this helix upon bilayer binding (*38*). Recently, we reported on the membrane topology of both helices 1 and 2 of colicin E1 in the closed channel state (absence of a membrane potential) and found that these helices retain their α helical character and length, even when bound at the surface of large unilamellar vesicles (*39*, *40*).

Herein, we continue our investigation of the membrane-bound topology of the helices within the closed state of the colicin E1 channel with a study of the membrane-bound disposition of helix 3 (Val-386−Leu-400). Using site-directed fluorescence labeling of a series of cysteine mutants coupled with rigorous analysis involving various fluorescence techniques, we found that helix 3 is also an amphipathic α helix. However, upon bilayer association, helix 3 becomes extended compared to its length within the soluble protein structure, and it lays tightly appressed to the membrane surface while adopting a slightly tilted disposition with its N-terminus more deeply buried within the bilayer than the C-terminus. The fluorescence data suggest that helix 3 extends from Ile-383 to Lys-402 in the membrane-bound, closed channel state of the channel peptide.

EXPERIMENTAL PROCEDURES

Materials. All chemicals, unless otherwise stated, were purchased from Sigma (Oakville, ON). All steady-state fluorescence measurements were collected using a PTI-Alphascan-2 spectrofluorimeter (Photon Technologies Inc., South Brunswick, NJ) equipped with a thermostated cell holder. All measurements are reported as the mean ± standard deviation and were performed at least in triplicate.

Mutagenesis, Protein Purification, and Monobromobimane Labeling. Cysteine-scanning mutagenesis, in which each amino acid residue from Lys-381 to Ser-405 of P190H$_6$[1] was individually replaced with a cysteine, was performed using the Stratagene (La Jolla, CA) Quikchange mutagenesis kit. Plasmid DNA was purified using the High Pure Plasmid isolation kit from Roche Diagnostics (Laval, QC). Wild-type (WT) P190H$_6$ and Cys mutant proteins were prepared and purified from transformed lexA$^-$ *E. coli* IT3661 cells as previously described (*39*). The purity of each protein was assessed by SDS−PAGE. The protein concentration was determined by absorption spectroscopy at OD$_{280}$, using the extinction coefficient (ϵ) of 28 590 M^{-1} cm^{-1} (ϵ = 27 310 M^{-1} cm^{-1} for the Tyr mutant protein, Y396C) (*37*). Purified mutant proteins were labeled with monobromobimane (mBBr) (Molecular Probes, Eugene, OR) at a 20:1 molar ratio (probe: protein), and the labeling efficiency was determined as previously described (*39*).

Preparation of Large Unilamellar Vesicles (LUVs). 1,2-Dioleoyl-*sn*-glycero-3-phosphocholine/1,2-dioleoyl-*sn*-glyerco-3-[phospho-*rac*-(1-glycerol)] vesicles (60:40 molar ratio) (Avanti Polar Lipids, Alabaster, AL) were prepared and quantified as described previously (*39*), except the buffer used to resuspend vesicles consisted of 10 mM DMG and 100 mM NaCl (pH 4.0). Asolectin (Fluka, Oakville, ON) was purified according to the method of Schendel and Reid (*41*), and vesicles were prepared as described previously (*42*). The phospholipid concentration was determined using the microBartlett assay (*39*).

Steady-State Intrinsic Trp Fluorescence. The folding properties of all proteins were examined using intrinsic Trp fluorescence as previously described (*39*). Briefly, WT P190H$_6$ and unlabeled as well as bimane-labeled mutant proteins were diluted to 4 μM in PBS [50 mM NaH$_2$PO$_4$, 50 mM Na$_2$HPO$_4$, and 100 mM NaCl (pH 7.0)]. Intrinsic Trp residues were excited at 295 nm (excitation slit width of 2 nm), and emission was detected from 305 to 450 nm (slit width of 4 nm). The resulting traces were corrected for the buffer and wavelength-dependent bias of the emission components of the spectrofluorimeter before calculation of the λ emission maximum ($\lambda_{\mathrm{em,max}}$) from the first derivative of the smoothed spectra.

6-Methoxy-N-(3-sulfopropyl)quinolinium Assay for in Vitro Channel Activity. The 6-methoxy-*N*-(3-sulfopropyl)quinolinium (SPQ) assay was performed as described previously (*42*) using a Cary Eclipse spectrofluorimeter (Varian Instruments, Mississauga, ON). All buffers were at pH 5.0, and the extravesicular buffer consisted of 100 mM KCl and 10 mM DMG. The final protein concentration was 4 μg/mL.

Bimane Fluorescence Emission Spectra. The steady-state bimane fluorescence emission spectra of all mutant proteins were measured as previously described (*39*). All measurements were taken with a 4 μM protein sample in DMG buffer

---

[1] Abbreviations: bimane-Cys, bimane-labeled *N*-acetylcysteine; CSM, cysteine-scanning mutagenesis; P190H$_6$, colicin E1 190-residue channel domain with an N-terminal six-histidine tag; DMG, dimethylglutaric acid; DTT, dithiothreitol; DOPC, 1,2-dioleoyl-*sn*-glycero-3-phosphocholine; DOPG, 1,2-dioleoyl-*sn*-glycero-3-[phospho-*rac*-(1-glycerol)]; HPSA, helical periodicity surface analysis; LUVs, large unilamellar vesicles; mBBr, monobromobimane; PBS, phosphate-buffered saline; $\lambda_{\mathrm{em,max}}$, fluorescence wavelength emission maximum; *Q* ratio, ratio of quenching by KI to that by 10-DN; rpt, residues per turn; SASA, solvent accessible surface area; SPQ, 6-methoxy-*N*-(3-sulfopropyl)quinolinium; WT, wild-type.

[20 mM dimethyl glutarate and 130 mM NaCl (pH 4.0)] in the presence or absence of excess LUVs (800 μM, final concentration). The data were corrected for the buffer and wavelength-dependent bias of the equipment (*36*) before calculation of the $\lambda_{em,max}$ from the first derivative of the smoothed spectra.

Solvent Accessible Surface Area (SASA). To correlate the bimane fluorescence parameters with the local environment of each probed site, the solvent accessible surface area of each helix 3 amino acid side chain was determined using a Web-based program called GETAREA 1.1 (*43*) with a 1.4 Å water probe after input of the crystal structure coordinates of P190H$_6$ (PDB entry 2I88) (*23*).

Steady-State Bimane Fluorescence Anisotropy. The steady-state fluorescence anisotropy (r) measurements were taken using "T-format" detection by simultaneously comparing the intensities of the vertically (I_{VV}) and horizontally (I_{VH}) polarized emitted light when the sample was excited with a vertically polarized light as previously described (*39*).

Dual Quenching Analysis. Depth-dependent quenching of membrane-bound bimane-labeled mutant proteins was performed as described previously (*44*). To measure iodide quenching (F_{KI}), the fluorescence of samples was measured on a PTI Alphascan-2 spectrofluorimeter in ratio mode using semi-micro quartz cuvettes (0.5 cm × 0.5 cm) containing 100 μM LUVs and 7.5 μg of protein or LUVs only (background). F_{KI} was determined after the addition of a 50 μL aliquot of an aqueous solution from a 1.7 M KI and 0.85 mM $Na_2S_2O_3$ stock solution. The fluorescence values after KI addition were corrected for dilution before quenching was calculated. The excitation wavelength was set at 375 nm while the emission intensity was observed at 467 nm. The excitation and emission slit widths were 2.5 and 5.0 nm, respectively. To measure the efficiency of 10-doxylnonadecane (10-DN) quenching, membrane-bound protein or vesicles lacking protein were prepared as described above except that the 10-DN quencher-containing LUVs contained 10 mol % 10-DN. After preparation, all the samples were allowed to equilibrate for 30 min at 24°C before the measurement of initial fluorescence.

Calculation of the Iodide:10-DN Quenching Ratio (Q Ratio). The ratio of quenching by 10-DN to that by KI (Q ratio) was used to determine the depth of bimane in lipid bilayers as described previously (*40*).

Sensitivity of the Fluorescence Parameters of Bimane to Solvent Polarity. The sensitivity of bimane fluorescence to solvent polarity was assessed using *N*-acetylcysteine conjugated with bimane (bimane-Cys) as a probe. Bimane-Cys was produced by reacting mBBr with a 10-fold molar excess of *N*-acetylcysteine in 100 mM NH_4HCO_3 buffer (pH 8.1) for 1 h. The reaction mixture was lyophilized overnight and subsequently resuspended in dioxane/water mixtures of 0−100% (v/v) dioxane. The fluorescence emission and lifetime of bimane-Cys (2 μM bimane-Cys) samples in dioxane/water mixtures with different dielectric constants ($\epsilon = 2.3-80$) were determined.

Prediction of Secondary Structure from Fluorescence Parameters. The secondary structure elements were predicted from the observed fluorescence parameters using a method adopted from Cornette and colleagues (*40*, *45*). In brief, the periodicity and the angular frequency of the observed fluorescence parameters were obtained through a least-squares fitting approach using the harmonic wave function:

$$y = a \sin\left[2\pi\left(\frac{x+b}{p}\right)\right] + c \qquad (1)$$

where a is the amplitude, b is the phase, p is the period, and c is an offset value. The estimates of a, b, c, and p were initially obtained using four different methods of nonlinear least-squares fit in the Statistical Analysis System (SAS) version 9.1 statistical software package (SAS Institute, Cary, NC). The power spectra of the measured bimane fluorescence $\lambda_{em,max}$ were calculated using the method developed by Cornette and colleagues (*45*).

RESULTS

Protein Expression, Purification, Activity, and mBBr Labeling. The region within the colicin channel domain that encompasses helix 3 of the soluble protein (Lys-381−Ser-405) was subjected to cysteine-scanning mutagenesis (CSM), and this segment is shown by the downward-facing bracket in Figure 1A. All the single Cys mutations were performed on the WT P190H$_6$ peptide which possesses a single Cys residue (Cys-505) that is buried deep within the core of the soluble protein and is unreactive to thiol-modifying reagents unless the protein is denatured (*46*). The spatial disposition of the mutation sites within the soluble protein is shown in Figure 1B by the labeled spheres corresponding to the α carbon of each residue. As observed in panels A and B of Figure 1, the protein segment under investigation contains the entire helix 3 as well as the loop regions immediately preceding and following this helix.

All the mutant proteins were expressed at acceptable levels, producing on average, a yield of 20−30 mg/L of cell culture, except for mutants F393C, Y396C, and L400C, for which the expression level was between 2 and 3 mg/L. All mutant proteins were purified to at least 95% homogeneity as assessed by SDS−PAGE. Interestingly, these three residues (Phe, Tyr, and Leu) are largely buried in the crystal structure of the soluble protein, with 0, 8.04, and 0.01 Å^2 solvent accessible surface areas (SASA), respectively, as opposed to 25.6−165 Å^2 for the other residues (Figure 2B). Therefore, a possible explanation for the reduced yield of these mutants could be the protein packing effects caused by Cys replacement. In support of the idea, the Trp fluorescence emission maxima (Trp $\lambda_{em,max}$) for these three mutants were red-shifted compared with those of the WT protein (331, 331, and 329 nm, respectively, compared with 324 nm for the WT), indicating that the structural integrity of these proteins was compromised to some degree (Table 1). All other single-Cys mutants had Trp $\lambda_{em,max}$ values similar to that of the WT protein (Table 1). Furthermore, the channel forming activities of these mutants (tested using the SPQ assay) were not impaired, ranging from 86 to 100% of the activity of the WT protein for F393C, Y396C, and L400C (Table 1). Overall, the relative channel forming activities of the various Cys mutant proteins ranged from 83 to 118% of the WT activity (Table 1).

The mBBr labeling efficiency, which is the fraction of each mutant channel protein that is labeled with bimane (no label, 0%; complete labeling, 100%), is shown in Figure 2A. Most mutants exhibited a labeling efficiency between 60 and

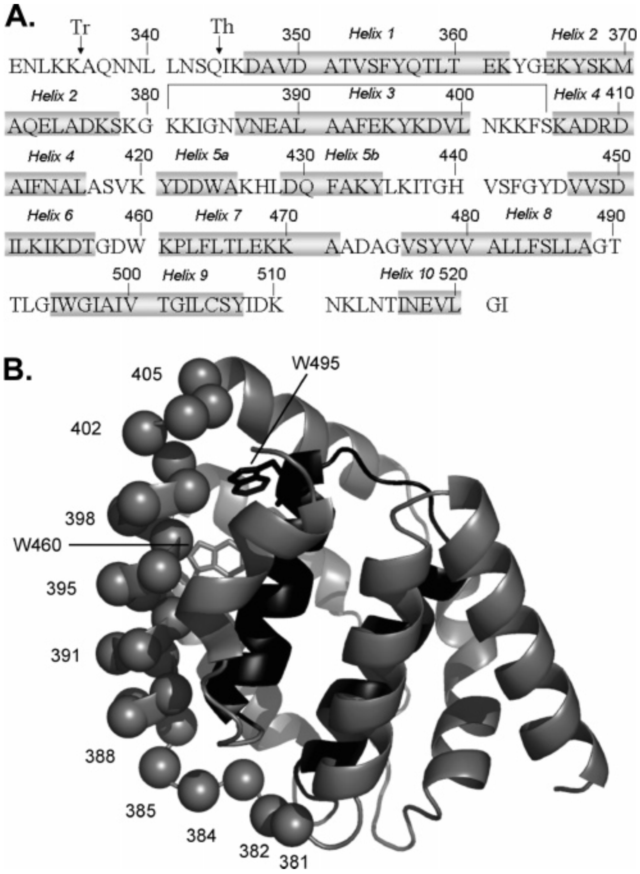

FIGURE 1: Schematic representation of the secondary and tertiary structures of colicin E1. (A) Primary sequence and secondary structure of the channel-forming domain of the colicin E1 P190 channel protein. Residues in the downward-facing bracket are those corresponding to Cys substitutions. The tryptic and thermolytic digestion sites of P190 are indicated by the arrows and the labels Tr and Th, respectively. The secondary structure of P190 is based on the 2.5 Å crystal structure of P190 (*23*) (PDB entry 2I88). (B) Ribbon topology of the 2.5 Å crystal structure of the P190 peptide. Hydrophobic helices 8 and 9, which serve as a membrane-anchoring hairpin in the membrane-associated state, are colored black. The positions of the Cys mutation sites are highlighted with residue numbers and/or spheres that correspond to the α-carbon of each substituted residue. Also highlighted are the side chains (stick format) of Trp-460 and Trp-495.

100%, values which correlate with our previous results for helices 1 and 2 of P190H$_6$ (*39*, *40*). However, the three poorly expressing mutants, F393C, Y396C, and L400C, exhibited slightly elevated labeling efficiencies (118, 115, and 123%, respectively). To understand the root cause(s) behind these elevated values, we compared the labeling efficiencies of the mutants with their solvent accessibility (SA) values (Figure 2A). Predictably, a correlation between labeling efficiency and solvent accessibility was seen for the residues that are classified as solvent-exposed (SA > 50%), but interestingly, residues that are largely buried and solvent inaccessible (SA < 20%) did not have a corresponding decrease in labeling efficiency. However, theoretically, the labeling efficiency should not exceed 100%, and thus an efficiency greater than 100% indicates a degree of nonspecific labeling, which may originate from an enhanced accessibility of the bimane reagent to the core of the channel peptide where the completely buried and native Cys residue, Cys-505, resides. Importantly, even for these proteins, the labeling efficiency never exceeded 118%.

Membrane Orientation of the Helix 3 Segment. The membrane orientation of the helix 3 segment upon binding with lipid vesicles was assessed through measurement of the bimane fluorescence emission maximum (bimane $\lambda_{em,max}$) of each mutant. To evaluate the reliability of our bimane $\lambda_{em,max}$ measurements, we compared the profile of the measured bimane $\lambda_{em,max}$ of the mutants in aqueous medium with their corresponding SASA values (Figure 2B). Apparently, the bimane $\lambda_{em,max}$ values correlated well with the SASA values of the residues. For instance, solvent-exposed residues such as Lys-382, Asn-385, Asn-387, Glu-388, Lys-395, Asp-398, and Lys-402, which possess SASA values of >70 Å^2, also exhibited red-shifted bimane $\lambda_{em,max}$ values ($\lambda_{em,max}$ > 470 nm). In contrast, buried residues such as Val-386, Ala-389, Ala-392, Lys-397, and Leu-400 with SASA values of <30 Å^2 displayed blue-shifted bimane $\lambda_{em,max}$ values ($\lambda_{em,max}$ < 470 nm). A slight disharmony in the correlation occurred at the two loop regions (Lys-381−Asn-385 and Asn-401−Ser-405). This can be reconciled by the fact that the loop regions are generally more flexible than helical segments (helix 3), and these loops would be expected to adopt a series of conformations.

To probe the apparent polarity of the local environment around each residue within the helix 3 segment, the bimane $\lambda_{em,max}$ values of the mutants in the membrane-bound state were converted to apparent polarity (ϵ) values using a standard polarity curve ($\lambda_{em,max} = 0.33\epsilon + 452.8$) generated previously in our lab (*39*) using a bimane-*N*-acetyl-Cys model compound in a series of dioxane/water mixtures with known ϵ values. The apparent polarity value for each mutant is shown in Figure 2C. These data reveal that the apparent polarity for the residues within the helix 3 segment oscillates from an ϵ of 25.8 (K381C) to an ϵ of 71.2 (K402C), indicating that this peptide segment is located largely at the interfacial layer of the membrane, where the head groups of the lipids meet with the aqueous medium and the dielectric constant likely ranges from 20 to 80 (*47*, *48*). The bimane-labeled residues K381C, N385C, A389C, K397C, L400C, N401C, and K403C have low dielectric constants (ϵ < 30), and thus, they are predicted to be in close contact with the head groups of the lipid bilayer, likely partially bathing in the hydrophobic sea of alkyl chains of the membrane. The bimane-labeled residues with higher dielectric constants (ϵ > 65) such as K382C, E388C, K395C, and K402C (Figure 2C) are predicted to be more solvent-exposed. The fact that the apparent polarity values for the mutants oscillate along the axis where $\epsilon = 48.2$ (Figure 2C) indicates that the helix 3 segment most likely associates peripherally with the membrane surface.

Site-Specific Probe Mobility and Protein−Lipid Interactions. The fluorescence anisotropy (*r*) of each bimane-labeled residue was measured in both the soluble and membrane-bound states (Figure 2D). Anisotropy (*r*) is inversely dependent upon the rotational freedom of the fluorescent probe in a nonviscous medium. Therefore, probe mobility (1/*r*), calculated as the inverse of anisotropy, was plotted in Figure 2D as a more intuitive measure of the rotational freedom of bimane tethered at various sites along the helix 3 segment of the channel peptide. As expected, the site-specific probe mobility values oscillated in a wavelike pattern for both the soluble and membrane-associated states, reflecting the helical nature of the helix 3 segment even when

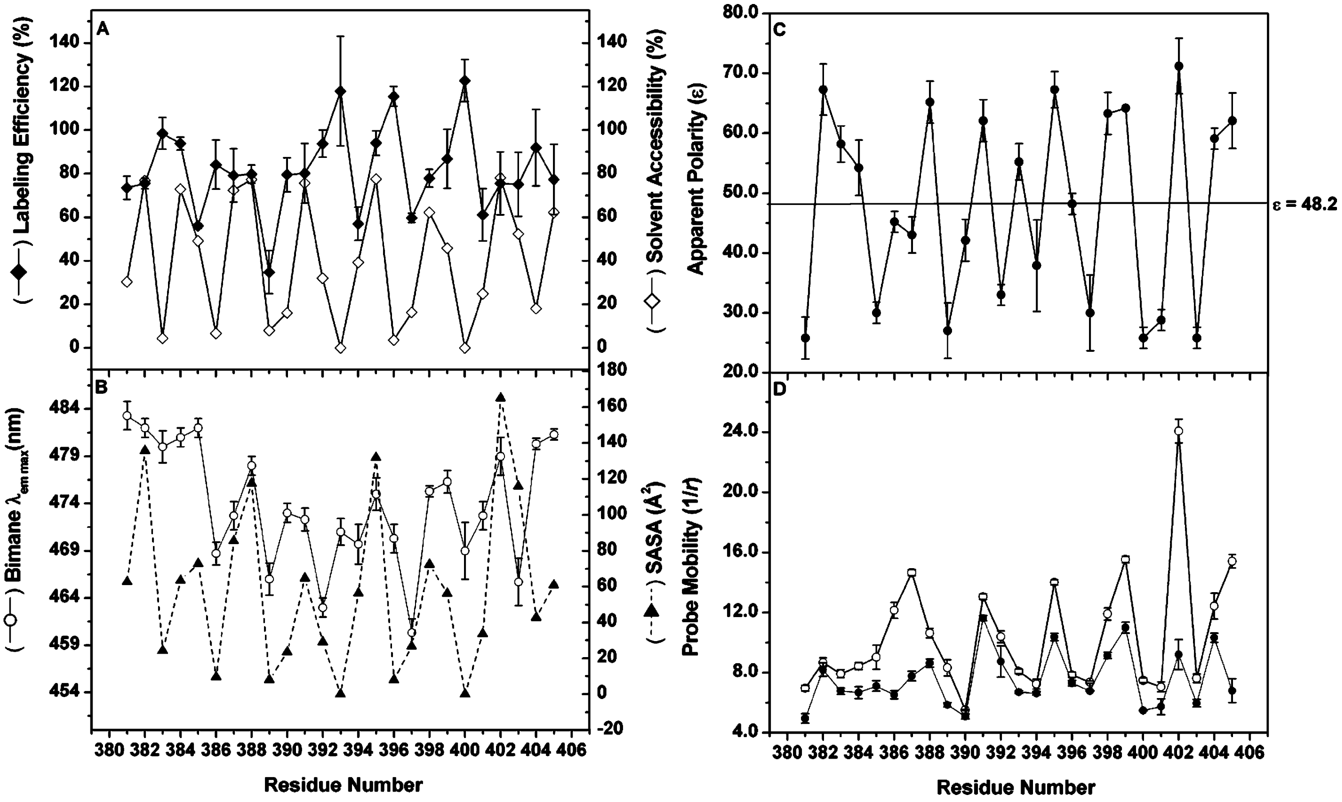

FIGURE 2: Labeling efficiency, bimane fluorescence emission maxima ($\lambda_{em,max}$), probe mobility, and apparent polarity of the bimane-labeled Cys mutants in the P190H$_6$ peptide. (A) Labeling efficiency (◆) and corresponding side chain solvent accessibility (◇) of the bimane-labeled cysteine residues. The side chain solvent accessibility (SA) was calculated from the coordinates of the 2.5 Å crystal structure of the P190 peptide by using a 1.4 Å probe as described in Experimental Procedures. (B) Bimane $\lambda_{em,max}$ (○) of the cysteine mutants in the soluble state and corresponding side chain SASA values (- - -) of the residues. Solvent accessible surface areas are calculated as described in Experimental Procedures. Average values and standard deviations of bimane $\lambda_{em,max}$ from at least triplicate measurements are shown. (C) Membrane-associated apparent polarity in terms of the ϵ values (●) of the bimane-labeled cysteine mutants. The apparent polarity is calculated from the measured bimane $\lambda_{em,max}$ of the mutants in the membrane-associated state using a standard polarity curve of $\lambda_{em,max} = 0.33\epsilon + 452.8$ (*39*). Average values and standard deviations from at least triplicate measurements are also shown. Additionally, shown as a horizontal line is the axis where $\epsilon = 48.2$, which is the center of the oscillation of the apparent polarity values. (D) Probe mobility of bimane-labeled Cys mutants of the colicin E1 channel domain. Probe mobility is calculated as the inverse of the observed fluorescence anisotropy. The probe mobility values of the bimane-labeled Cys mutants in the soluble state are shown as white circles. The probe mobility values for the membrane-associated state of the channel domain are shown as black circles. Average values and standard deviations for at least triplicate measurements are shown.

bound to the membrane bilayer. Furthermore, the patterns of the two curves shown in Figure 2D are similar, indicating that the segment does not undergo a significant conformational change as it binds to the lipid vesicles. However, it should be noted that the factors influencing probe mobility in an aqueous medium are different from those in a membrane-associated state. In the aqueous solvent, probe mobility is mainly affected by the location of the bimane chromophore with respect to the tertiary structure of the protein (i.e., solvent-exposed or buried). Accordingly, the calculated probe mobility of bimane tethered to residues within the segment from Lys-381 to Ser-405 in the soluble state (Figure 2D) correlates well with their respective SASA values (Figure 2B). Residues that are predicted to be surface-exposed (with a SASA of >70 Å^2), such as N387C, K395C, and K402C, have greater probe mobility ($1/r > 12.0$) than the rest of the residues within this protein segment. The remarkably high probe mobility of K402C [$1/r = 24$ (Figure 2D)] may be attributed to the combined effects of a highly solvent exposed location [SASA = 165 Å^2, highest among all the residues (Figure 2B)] as well as the predicted depolarization of anisotropy by the radiation-less energy transfer to nearby Trp residues [the distances between the K402C bimane-labeled residue and Trp-460 and Trp-495 are 13.5 and 14.1 Å, respectively, as measured on the basis of the P190 X-ray structure (Figure 1B)]. Radiation-less energy transfer, or fluorescence resonance energy transfer (FRET), is considered an effective mechanism for anisotropy depolarization as one single step of resonance energy transfer can reduce the anisotropy to 4% of its initial value (*49*).

In the presence of LUVs, bimane probe mobility is mainly affected by interactions with the lipid given the high viscosity of the membrane compared with that of the aqueous solution, although the peptide rate of tumbling in solution will decrease upon binding the much larger vesicle structure. Supporting this theory, probe mobility values for all the bimane-tethered residues decreased when the channel peptide associated with the lipid vesicles, indicating that the probes were largely immobilized by the membrane. Residues in closer contact with the membrane, as suggested by their lower apparent polarity values ($\epsilon < 40$) (Figure 2C), include K381C, N385C, A389C, E394C, K397C, L400C, N401C, and K403C. These residues exhibited relatively low probe mobility [$1/r < 7.0$ (Figure 2D)], suggesting that there is a reasonable correlation between probe mobility and apparent ϵ values. Residues with higher apparent polarity values ($\epsilon > 60$), such as K382C,

Table 1: Summary of the Fluorescence Measurements of Unlabeled or Labeled Wild-Type and Helix 3 Cys Mutants of the Colicin E1 Channel Domain

	Trp $\lambda_{em,max}$ (nm)[a]		
P190H$_6$	unlabeled	labeled	relative activity (%)[b]
WT	324.3 ± 0.6		100 ± 12
K381C	325.3 ± 1.5	323.7 ± 0.6	118 ± 3
K382C	322.7 ± 1.2	323.3 ± 0.6	107 ± 5
I383C	326.3 ± 1.2	323.7 ± 0.6	107 ± 8
G384C	325.0 ± 1.0	326.7 ± 1.5	107 ± 10
N385C	323.7 ± 1.2	324.0 ± 1.0	105 ± 8
V386C	324.3 ± 1.5	326.3 ± 2.5	100 ± 7
N387C	324.3 ± 0.6	324.3 ± 2.1	103 ± 9
E388C	324.0 ± 1.7	325.0 ± 1.0	115 ± 3
A389C	324.3 ± 2.3	323.0 ± 0.1	112 ± 9
L390C	323.3 ± 1.2	324.7 ± 0.6	102 ± 8
A391C	324.7 ± 1.2	323.3 ± 1.5	102 ± 10
A392C	323.7 ± 1.2	325.3 ± 1.2	92 ± 3
F393C	331.3 ± 0.6	331.7 ± 0.7	86 ± 15
E394C	324.7 ± 1.7	322.3 ± 0.7	93 ± 2
K395C	324.0 ± 1.6	323.0 ± 1.0	83 ± 4
Y396C	331.3 ± 0.6	332.5 ± 2.1	101 ± 6
K397C	325.0 ± 0.0	326.7 ± 2.1	100 ± 4
D398C	322.7 ± 0.6	322.0 ± 2.6	101 ± 8
V399C	325.0 ± 0.0	321.0 ± 1.0	101 ± 13
L400C	329.7 ± 1.5	331.7 ± 0.6	100 ± 5
N401C	327.3 ± 0.6	328.7 ± 1.2	109 ± 7
K402C	322.7 ± 0.6	324.3 ± 1.2	95 ± 4
K403C	322.3 ± 2.1	322.7 ± 1.2	103 ± 13
F404C	324.3 ± 0.6	326.3 ± 1.8	101 ± 7
S405C	323.3 ± 0.6	324.7 ± 1.1	90 ± 2

[a] Values shown are mean ± the standard deviation for at least triplicate measurements. [b] A channel activity of 100% represents the WT P190H$_6$ pore forming ability that can release 70% of the encapsulated SPQ dye from the asolectin LUVs.

E388C, A391C, K395C, D398C, V399C, K402C, and F404C, also displayed higher probe mobility values [1/*r* > 7.0 (Figure 3)]. The large decrease in probe mobility of K402C upon binding to LUVs (1/*r* = 9.2 in the LUVs compared with 1/*r* = 24.1 in the aqueous solvent) can likely be attributed to the unusually high mobility of the bimane probe for the soluble state of the peptide as well as the alleviation of anisotropy depolarization by FRET upon membrane binding.

Membrane Penetration Depth of the Helix 3 Segment. The novel dual-fluorescence quenching method pioneered by the London group (*44*, *50*, *51*) is tailored to measure membrane penetration depth of a protein upon binding with a lipid membrane (*39*, *40*, *52*). This method involves the measurement of fluorescence quenching by two different quenchers, KI and 10-DN, which specifically quench solvent-exposed probes and membrane-embedded probes, respectively. The ratio of the quenching, called the *Q* ratio, is linearly dependent on the depth of the residues within the membrane (*50*); thus, it is used as a relative scale to compare the differences in membrane penetration depth for a fluorescent probe. Low *Q* ratio values indicate the probe is quenched more by KI and less by 10-DN and are therefore localized outside the membrane. Similarly, high *Q* ratio values indicate significant membrane depth penetration of the probe into the bilayer away from the water soluble quencher, KI (*39*, *40*, *44*, *50*, *51*). The dual-fluorescence quenching method has been used to study diphtheria toxin (DT) A chain (*44*, *50*−*52*) and helices 1 and 2 in the channel domain of colicin E1 (*39*, *40*).

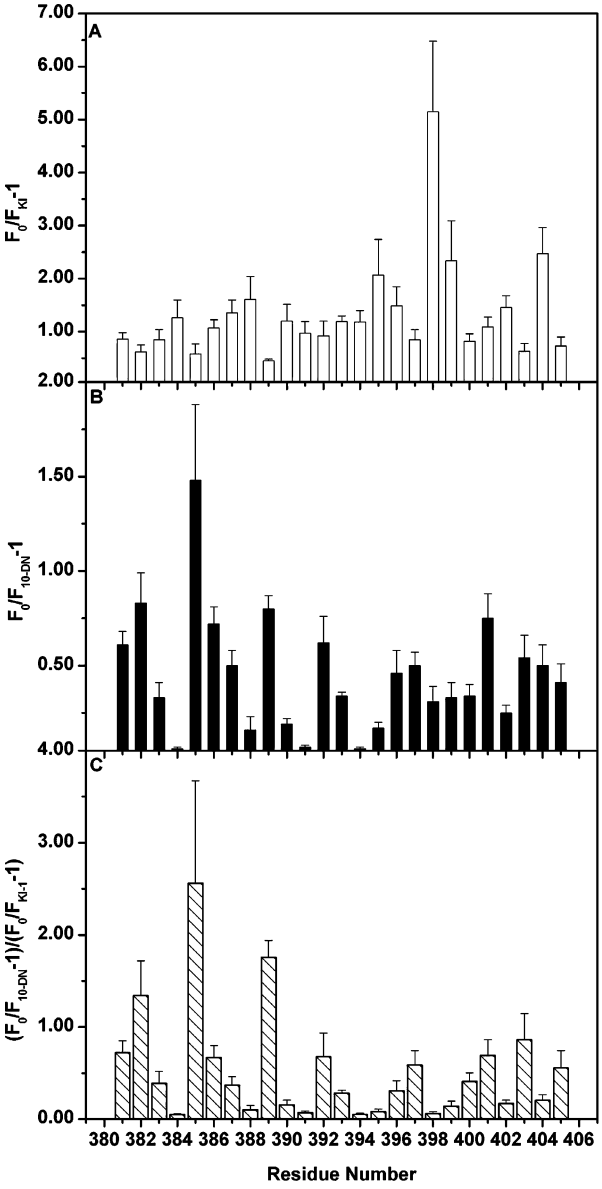

FIGURE 3: Membrane penetration depth for the Cys mutants of the colicin E1 channel domain in large unilamellar vesicles. (A) The histogram shows bimane fluorescence quenching by KI (white bars). F_0/F_{KI} is the ratio of fluorescence in the absence of KI (F_0) to that in the presence of KI (F_{KI}). (B) The histogram shows fluorescence quenching by 10-DN (black bars). F_0/F_{10-DN} is the ratio of the fluorescence of bimane in the absence of 10-DN to that in the presence of 10-DN. (C) The histogram shows the *Q* ratio of quenching by 10-DN to that by KI. The higher the *Q* ratio, the deeper the residue is inserted into the lipid bilayer. Average values and standard deviations from triplicate measurements are shown.

Figure 3 shows the fluorescence quenching data for KI (Figure 3A) and 10-DN (Figure 3B) as well as the calculated *Q* ratio (Figure 3C) for the helix 3 segment within the P190H$_6$ peptide in LUVs. Overall, it was seen that the helix 3 segment was quenched more effectively by KI than 10-DN, since the quench values were considerably higher when KI was the bimane quencher species. The *Q* ratio data indicate that the helix 3 segment was only peripherally associated with the membrane surface, consistent with the results of bimane $\lambda_{em,max}$ (apparent ϵ values) and probe mobility measurements. Residues with lower *Q* ratio values such as G384C, E388C, A391C, E394C, K395C, and D398C

Table 2: Summary of the Secondary Structure Analysis of the Lys-381−Ser-405 Segment of the Colicin E1 Channel Domain by HPSA

	parameter estimates from HPSA						
fluorescence parameter	a(SE)[a]	b(SE)[a] (deg)	c(SE)[a]	p(SE)[a] (rpt)	angular frequency (deg)	method[b]	residues[c]
bimane $\lambda_{\mathrm{em,max}}$ (soluble)	4.3(1.6)	343.4(35.7)	470.6(1.1)	3.8(0.2)	94.7	M	386−400
	4.0(1.6)	382.0(41.6)	470.0(1.1)	3.8(0.2)	93.8	GN	386−400
bimane $\lambda_{\mathrm{em,max}}$ (membrane)	3.8(1.4)	338.2(21.5)	468.7(1.0)	3.8(0.1)	95.5	GN	383−402
	3.8(1.4)	338.2(21.5)	468.7(1.0)	3.8(0.1)	95.5	M	383−402
1/r (soluble)	4.0(1.0)	382.0(26.7)	10.0(0.7)	3.8(0.1)	93.8	G	386−400
	4.0(1.0)	360.8(25.1)	10.4(0.7)	3.9(0.1)	92.5	GN	386−400
1/r (membrane)	1.0(0.5)	382.0(36.5)	8.0(0.4)	4.0(0.2)	90	G	383−402
	0.4(0.2)	380.0(28.9)	0.5(0.1)	4.0(0.2)	90	G	383−402
Q ratio (membrane)	0.5(0.2)	323.2(17.4)	0.5(0.1)	3.7(0.1)	97.3	M	383−402
	0.5(0.2)	323.2(17.4)	0.5(0.1)	3.7(0.1)	97.3	GN	383−402

[a] The a, b, c, and p parameters refer to those used in eq (1). SE is the estimated standard error of each parameter. [b] The four methods of nonlinear least-squares fit used in this research are gradient (G), Gauss−Newton (GN), Marquardt (M), and Newton (N). [c] The sequence ranges include those residues from the helix 3 segment that were included in the fitting analysis.

are considered to be largely solvent-exposed; residues with higher Q ratio values such as K382C, N385C, A389C, N401C, and K403C are thought to be buried within the interfacial layer of the membrane. Interestingly, while the fluorescence quenching of the tethered bimane probe varies along the segment in a wavelike pattern implying the amphipathic helical nature of the segment, fluorescence quenching by KI (Figure 3A) was stronger at the C-terminal half of the helix (residues K395C−S404C). In contrast, quenching by 10-DN (Figure 3B) was generally stronger in the N-terminal half of the segment (residues K381C−F393C). Therefore, not surprisingly, the Q ratios are generally higher in the N-terminal half of the helix 3 segment than those of the C-terminal half (Figure 3C). These observations are consistent with helix 3 possessing a slightly tilted topology, appressed to the membrane surface and lying in the interfacial layer of the membrane with its N-terminal half slightly more buried than the C-terminal half of the segment.

Secondary Structure Analysis of the Segment in LUVs. Secondary structure analysis deduced from the bimane fluorescence parameters is based on the following considerations. First, it has long been accepted that a protein of organized structure within an anisotropic environment would be reflected in recognizable patterns in the chemical or physical properties of the residues in the protein. Second, because one turn of an α helix comprises between three and four residues (3.6 residues/turn), there will be a cyclic variation of the physical and chemical properties of the residues with a periodicity of 3.6−3.7 residues per turn (rpt) along any amphipathic α helix (*45*). Therefore, if the characteristic periodicity for an α helix is detected from the fluorescence parameters, it provides strong evidence that the secondary structure of the segment is indeed an amphipathic α helix. A method developed by Cornette et al. (*45*) to detect the periodicity within a putative amphipathic helical sequence has been adapted by our laboratory, and the data were analyzed with the SAS version 9 statistical software package (see Experimental Procedures) in a method that we call helix periodicity statistical analysis (HPSA). Basically, we fit the data for each fluorescence parameter calculated according to eq 1 using four different methods of nonlinear least-squares regression analysis (gradient, Gauss−Newton, Marquardt, and Newton), and the SAS program was used to calculate the best estimates of a, b, c, and p with standard errors.

Table 2 shows the summary of the secondary structure analyses of the helix 3 segment by our HPSA method. It is clear from the data that the HPSA method worked well for the bimane fluorescence parameters measured in the soluble state of the protein segment. The estimates of p (periodicity) for both bimane $\lambda_{\mathrm{em,max}}$ and 1/r mostly fell in the range of 3.6−3.7 rpt, suggesting an α helical structure for this segment in the aqueous medium. In the presence of LUVs (membrane-bound state), the confidence in the predicted parameters for an α helix increased and the α helical nature of the helix 3 segment became more convincing as indicated by the estimated p values from both the bimane $\lambda_{\mathrm{em,max}}$ and Q ratio data, which were closer to 3.6−3.7 rpt with smaller standard errors (Table 2). The estimated p values for bimane $\lambda_{\mathrm{em,max,}}$ and Q ratio measurements for the membrane-associated state of the helix 3 segment by both Gauss−Newton (GN) and Marquardt methods were 3.77 ± 0.11 and 3.70 ± 0.09, respectively, providing convincing evidence of the α helical nature of the helix 3 segment upon membrane binding. While the periodicity detected in the 1/r values deviated slightly from 3.6−3.7 rpt, upon consideration of the standard errors, the 1/r data provide support for the α helical nature of the segment (Table 2).

The nonlinear least-squares fit of bimane $\lambda_{\mathrm{em,max}}$ values for the membrane-associated helix 3 segment using the Gauss−Newton method was used as a statistical model to define the boundaries of the helix. The GN model of bimane $\lambda_{\mathrm{em,max}}$ in the presence of LUVs was favored because the normal quantile plot and the standardized residual plot (data not shown) both indicate that the GN model ($y = 3.8 \sin\{2\pi[(x + 338.2)/3.77]\} + 468.7$, where y is the bimane $\lambda_{\mathrm{em,max}}$ in nanometers and x is the residue number) fits the bimane fluorescence $\lambda_{\mathrm{em,max}}$ data very well. The normal quantile plot was used to assess whether the residuals of the bimane fluorescence $\lambda_{\mathrm{em,max}}$ data and the fit to the GN model followed the normal distribution. Ideally, the normal quantile plot would consist of points closely following a straight line passing through the origin, which is consistent with our data (not shown). The standardized residual plot was used to assess the quality of the fit to the model in the HPSA method. Since the standardized residuals of our data were randomly scattered and fall in the region of ±1.96 (the 95% confidence limit of a normal distribution, data not shown), it was concluded that the GN model of the fluorescence bimane $\lambda_{\mathrm{em,max}}$ data was valid. We employed the square of the residuals to show the deviation in the experimental fluorescence bimane $\lambda_{\mathrm{em,max}}$ data from the GN model and to help define the boundaries of helix 3 when bound to the membrane bilayer. Since the model is a harmonic wave function reflecting the helical pattern of the measured parameters, residues outside the helix should show more deviation than the residues harbored within the helix. Also, by using squared residuals, the calculated values become positive, and the difference in the deviations of each residue from the GN model are thus magnified, allowing for ease of statistical comparison.

Figure 4 shows the squared residual plots for the bimane fluorescence $\lambda_{\mathrm{em,max}}$ data of both the soluble and membrane-bound channel peptide. It is evident that our new method of defining the boundaries of an amphipathic α helix (helix 3) was supported by the data of the soluble peptide (Figure 4A). Residues V386C−L400C exhibited a significantly smaller deviation than residues in the remainder of the peptide, which correlates nicely with the known limits of helix 3 in the X-ray structure. In the membrane-bound state, the differences in the deviations between the residues at the N- and C-termini, and the intervening residues, were reduced compared with those in the soluble state. This phenomenon can be attributed to the blue-shifted bimane fluorescence $\lambda_{\mathrm{em,max}}$ values of the helix 3 residues upon peptide binding to the LUV surface. Nonetheless, it is still clear that the residues from I383C to K402C have smaller deviations than the rest of the segment, with only a few exceptions. Therefore, helix 3 in the membrane-bound channel domain is predicted to include the residues from Ile-383 to Lys-402. This observation is supported by the Fourier-transfer power spectrum analysis of the bimane fluorescence $\lambda_{\mathrm{em,max}}$ data (Figure 4C), a method developed by Cornette et al. (*45*). The angular frequency at which the intensity of the power spectrum reaches its peak is used to calculate the periodicity within the test sequence of numbers. In our case, the power spectrum showed a much more distinct peak for the bimane fluorescence $\lambda_{\mathrm{em,max}}$ data after removal from the analysis of the data for five residues (K381C, K382C, K403C, F404C, and S405C), considered to be outside the helix 3 boundaries on the basis of our bimane fluorescence parameters (Figures 2−4). The angular frequency of the segment from I383C to K402C was 96.5°, from which the periodicity of helix 3 was calculated to equal 3.73 rpt. This is in good agreement with the results from HPSA and further supports the hypothesis that upon membrane association, helix 3 elongates from V386C−L400C in the soluble protein to include residues Ile-383−Asn-385, Lys-401, and Lys-402 in the membrane-associated state.

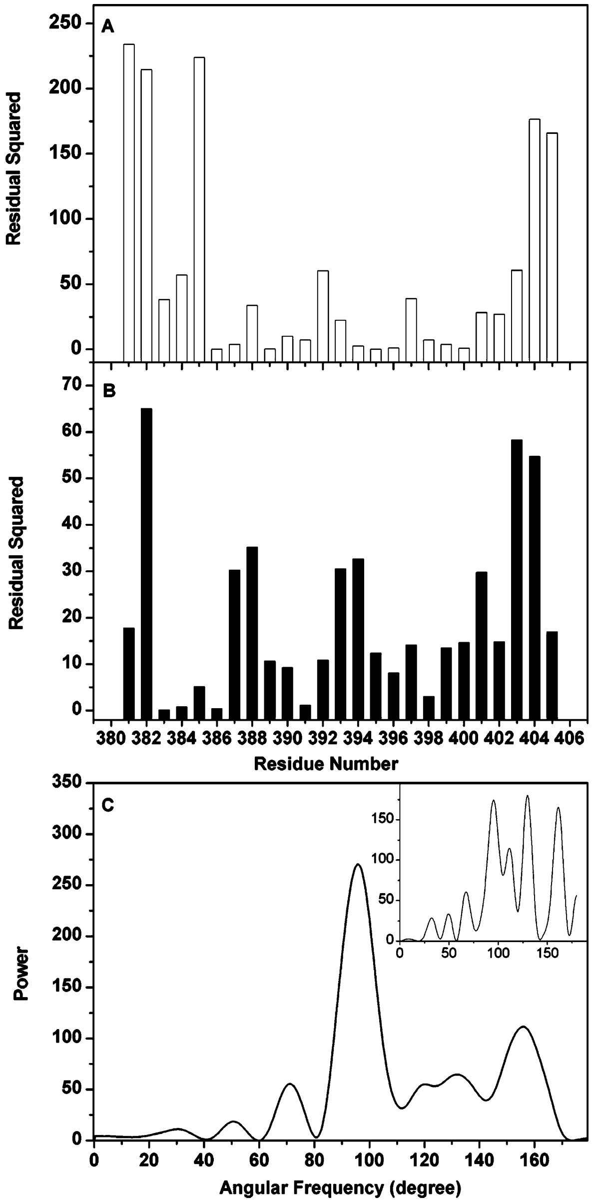

FIGURE 4: Squared residual plot and power spectrum of the bimane $\lambda_{\mathrm{em,max}}$ data. (A) Histogram that depicts the squared residuals between the soluble bimane $\lambda_{\mathrm{em,max}}$ data and the GN model (fit) of the soluble bimane $\lambda_{\mathrm{em,max}}$ data (white bars). (B) Histogram of the squared residuals for the membrane-associated bimane $\lambda_{\mathrm{em,max}}$ data and the GN model (fit) of the membrane-associated bimane $\lambda_{\mathrm{em,max}}$ (black bars). The heights of the bars indicate the deviation of the measured bimane $\lambda_{\mathrm{em,max}}$ data from the fit for the GN model for each measurement. (C) Fourier-transfer power spectrum of the measured bimane $\lambda_{\mathrm{em,max}}$ data in the membrane-bound state from I383C to K402C. The method of computing the Fourier-transfer power spectrum is described by Cornette et al. (*45*). Also shown in the inset is the Fourier-transfer power spectrum of bimane $\lambda_{\mathrm{em,max}}$ data along the whole segment from K381C to S405C. The angular frequency at which the power spectrum reaches its maximum intensity indicates the characteristic angular frequency of the sequence that can be converted to the periodicity using the equation $p = 360°/f$, where p is the periodicity and f is the angular frequency in degrees.

DISCUSSION

Previously, we showed that both helices 1 and 2 within the colicin E1 channel domain maintain their amphipathic α helical structures as well as the helical boundaries upon binding to the membrane surface in the closed channel state (at zero membrane potential) (*39*, *40*). The data pertaining to the helix 3 segment herein demonstrate that this helix is also an amphipathic α helix that lays on the membrane surface, but with a more pronounced tilt (embedded more deeply at the N-terminal end of the helix) (Table 2 and Figure 4). However, unlike helices 1 and 2, helix 3 elongates upon membrane binding from 15 residues in the soluble peptide to 20 residues in the membrane-bound state. Interestingly, the mutant proteins of the helix 3 segment were relatively insensitive to inactivation by Cys replacement mutagenesis and subsequent bimane labeling (Table 1). The greatest reduction in the in vitro channel activity for the helix 3 mutant proteins was only 17% (K395C mutant, Table 1), which supports previous mutagenesis studies that demon-

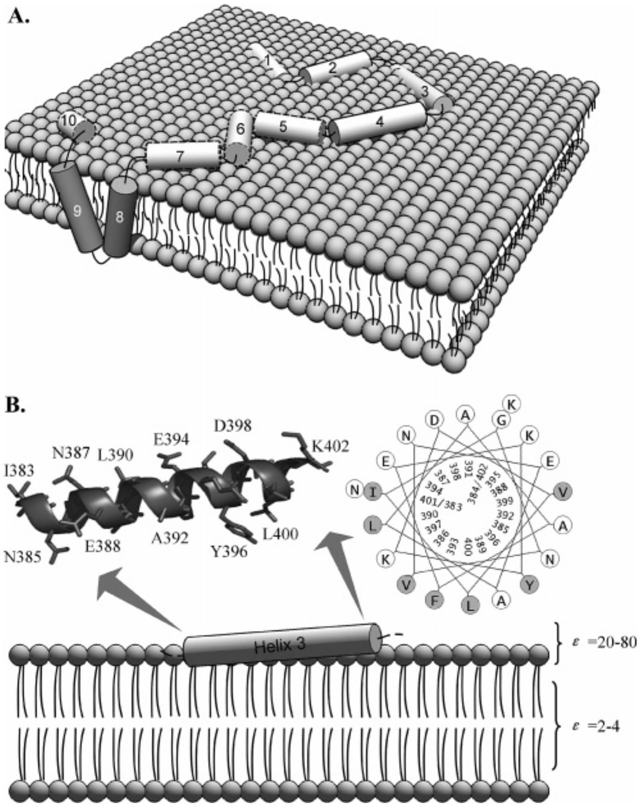

FIGURE 5: (A) Model of the membrane-bound topology of the colicin E1 channel domain. The 10 α helices of the colicin E1 channel domain are shown as cylinders with dark shading for helices 8 and 9. The general disposition of helices 1−4 is shown on the basis of previously published data (*38*−*40*) in combination with the data from this study, and the model is based on data at zero membrane potential. (B) Schematic representation of the membrane-bound topology of helix 3. Shown in the top panel is the ribbon diagram with residue side chains of the extended helix 3 from the channel domain oriented with the nonpolar face toward the bilayer hydrocarbon milieu of the bilayer and the polar face toward the aqueous solvent. Adjacent to the ribbon diagram is a helical wheel projection of the helix 3 segment (Ile-383−Lys-402) with the nonpolar residues that bathe within the bilayer shown as shaded circles. The bottom panel shows the relative membrane-bound topology of helix 3. Helix 3 lays on the surface of the membrane with its nonpolar face bathing the hydrocarbon portion of the bilayer, and its N-terminus is embedded more deeply with the membrane than its C-terminus. Also shown in the bottom panel are the theoretical dielectric constants (ϵ) of the interfacial layer (IF; $\epsilon = 20-80$) and the hydrophobic core of the acyl chain (HC; $\epsilon = 2-4$) (*47*, *48*).

strated the robust nature of the colicin E1 channel domain and its insensitivity to single-point mutations (*39*, *40*, *53*−*57*).

The site-directed fluorescence measurements presented herein provide compelling evidence for the amphipathic nature of helix 3 within the channel domain when it is bound to the membrane bilayer in the closed channel state at zero membrane potential (Table 1 and Figure 5). It is clear from the harmonic wave function analysis of helix 3 using the HPSA method that the periodicities and angular frequencies of residues within this helix do not change significantly upon binding to the membrane surface, implying that the integrity of this helix is maintained. The bimane fluorescence data suggest that helix 3 is appressed to the membrane surface with its nonpolar face bathing the hydrocarbon portion of the bilayer and its polar face interacting with the aqueous solvent. The helical wheel diagram illustrates the amphipathic nature of helix 3, and the bimane polarity data support the model shown in Figure 5 in which the nonpolar face bathes in the membrane (Ile-383, Asn-385, Val-386, Ala-389, Leu-390, Ala-392, Phe-393, Tyr-396, Lys-397, Val-399, and Leu-400) and the polar face (Gly-384, Asn-385, Asn-387, Glu-388, Ala-391, Glu-394, Lys-395, and Asp-398) interacts with water and/or the polar head groups of the phospholipids. The bimane fluorescence $\lambda_{\mathrm{em,max}}$, apparent polarity, relative mobility ($1/r$), and Q ratio (bilayer depth) data (Figures 2 and 3 and Table 2) indicate that helix 3 boundaries extend upon membrane association and that the ends of the helix are Ile-383 (N-terminus) and Lys-402 (C-terminus). This is consistent with earlier findings involving circular dichroism studies that revealed a net increase in the helicity of the channel domain upon membrane binding (*34*). Furthermore, analysis of the helix 3 sequence using AGADIR, which is a prediction algorithm that is based on helix/coil transition theory (http://www.embl-heidelberg.de /Services/Serrano/agadir/agadir-start.html), showed that the helix 3 segment (Gly-380−Ser-405) is predicted to markedly increase its helicity upon low-pH activation (31% increase from pH 7 to 4, data not shown). Additionally, adjacent residues on either end of the extended membrane-associated helix 3 [Ile-383−Lys-402 (Figure 1A)] did not fit the periodicity of an α helix (Figure 4B,C). Importantly, the connection between helices 2 and 3 is shortened by three residues upon membrane binding to include only Gly-380−Lys-382, while helix 3 likely terminates at Lys-402.

Previously, Salwinski and Hubbell (*38*) conducted an EPR study of the membrane-bound topology of the colicin E1 sequence from Lys-402 to Trp-424. They concluded that helix 4 elongates from residues 406−416 in the soluble peptide to residues 402−420 for the membrane-bound protein. However, the spin-label data for the peptide region from K402 to S405 showed some deviation from the expected periodicity of an α helix (*38*), and our data also indicate that this intervening region was likely not helical, even upon membrane association (Figures 2B,C and 4B). Furthermore, we fit the spin-label data from ref *38* using our HPFA method, and the results also indicated that the membrane-bound helix 4 likely begins at Lys-406 (data not shown). Importantly, these results fit the expected helical pattern for the membrane-bound colicin E1 channel domain when considering the findings for the membrane-bound lengths of helices 3 (Figures 2−4) and 4 (*38*). If upon membrane association helix 3 elongates to include helix 4, the result would be a helix with a minimum of 35 residues (Val-386−Lys-420), or possibly 39 residues (Ile-381−Lys-420) if one includes the N-terminal extension of helix 3. Additionally, Salwinski and Hubbell (*38*) proposed that helix 4 elongates upon membrane binding to include helix 5a, which implies that the resulting structure would form a monster helix totaling 44 residues. Such an extended helix structure is difficult to reconcile as part of the voltage-gated colicin E1 ion channel, although a protein segment in colicin Ia corresponding to helices 2−5 has been shown to be translocated across planar bilayers (*54*, *58*, *59*).

The dual quencher analysis data (Figure 3) provide a scan of the bilayer depth of the bimane fluorophore at each residue position within the helix 3 segment and therefore provides a comparison of the relative depths of the residues on the nonpolar face of helix 3 of the channel domain. However, one inherent weakness to our CSM method is that we replace the residue of interest with a Cys residue and then modify it with bimane. This removes (at the site of the bimane probe attachment) the effect of a charged or highly polar residue on the membrane disposition of our protein segment under investigation. The same argument applies for replacement of a large and nonpolar residue (Trp, Tyr, and Phe, for example) with Cys in the scrutinized protein element. Lys-382 is located within the "deep" region of helix 3 (Figure 3C), and this observation may, in fact, be masked because of the K382C mutation at this site. However, it is well-known that Lys residues (as well as Arg) can "snorkel" in proteins where its long side chain can reach up to the bilayer surface to allow the terminal, charged moiety to reside in the lipid head group region while the methylene groups of the residue are positioned well below the membrane−water interface (*60*, *61*). The *Q* ratio analysis revealed that the N-terminus of helix 3 is more deeply buried within the membrane bilayer than the C-terminus (Figure 3), and thus, this helix is tilted within the membrane, perhaps reflecting an interaction with another element within the channel domain. Importantly, the results from the *Q* ratio analysis were in excellent agreement with the $\lambda_{\mathrm{em,max}}$, apparent polarity, and relative mobility (fluorescence anisotropy) data for helix 3 (Figures 2 and 3 and Table 2), providing convincing evidence that helix 3 elongates and is bound to the surface of the membrane in a conformation roughly parallel to the bilayer surface and that it does not adopt a transmembrane orientation. Figure 5 is a simple model showing the membrane disposition of the three N-terminal helices of the channel domain in the closed channel state (zero membrane potential). It is clear that all three helices (helices 1−3) are amphipathic α helices that lay on the surface of the membrane parallel to the bilayer. Helix 1 is slightly more tightly appressed to the membrane surface than helix 2 with the N-terminus of helix 3 being embedded the deepest within the bilayer. The shallow nature of helix 2 corroborates previous proteolysis data of the membrane-bound colicin E1 channel domain that indicated the relative accessibility of helix 2 to protease digestion (*62*).

At present, the structure of the open channel formed by colicins upon voltage imposition has been controversial. It is generally believed that the voltage-gated, open channel consists of a single polypeptide with an even number of transmembrane helices having the N- and C-termini lying on the cis side of the membrane and involves the movement of surprisingly large segments of the membrane-bound precursor across the membrane. Less controversial is the identity of the anchor domain of the channel, which is generally believed to consist of helices 8 and 9 of the soluble protein. However, the identity of the remaining transmembrane segments of the open channel is less clear; various models have been proposed, most of which involve the formation of at least two additional transmembrane helices (*14*, *36*, *62*−*67*). A number of these models include an extended helix formed by the expansion of helices 1 and 2 of the soluble structure to provide one of the pillars of the open channel structure. Although helix rearrangements are an important aspect of the mechanism of colicin E1 membrane association, insertion, and pre-channel-state formation, our current data preclude the melding of helices 1 and 2 (and 3) into an extended helix as a feature of the closed channel state for colicin E1 (*39*) (Figure 5).

Our results to date (*39*, *40*) for helices 1−3 favor a toroidal model for colicin E1 as proposed previously by Cramer and co-workers (*14*, *66*) that involves the formation of the open channel with relatively short amphipathic helices (15−20 residues) that employ phospholipids in an inverted micellar conformation in forming a functional channel. Furthermore, it has recently been demonstrated that a much larger conductance channel (600 pS compared with 60 pS) may be formed in thicker bilayers and that colicin E1 may induce lipid "flip-flop" in such membranes (*67*). The toroidal lipid pore model has been used to describe the action of large toxins such as equinatoxin II (*68*) and sticholysin (*69*), antibiotic peptides (*70*, *71*), and apoptotic pore-forming proteins Bax (*72*) and tBid (*73*). An important requirement for the toroidal model is the sensitivity of the pore forming activity to membrane lipid curvature, where lipids with positive and negative spontaneous curvatures stimulate and inhibit pore formation, respectively. Cramer and co-workers (*66*) clearly demonstrated the sensitivity of colicin E1 pore forming activity to membrane curvature, lending support to the toroidal model for this bacteriocin and also the idea that the nature of the channel is influenced by the thickness of the membrane bilayer (*29*, *67*).

Our new HPSA method employing the harmonic wave function analysis approach of Cornette et al. (*45*) provides a more statistically rigorous approach to the definition of the length of membrane-associated amphiphathic α helices. Our future goal is to use this powerful new approach to scan the membrane topology of the "voltage sensor" (*63*) and "pH trigger" (*42*, *74*) regions of the colicin E1 channel domain. Obviously, considerable controversy about the nature and structure of both the closed and open states of the pore-forming colicins still exists. We will continue our pursuit of the membrane-bound topology of the closed state of colicin E1 through a residue-by-residue analysis using our fluorescence-based methodology. It is anticipated that in the near future we will also be able to study the membrane-bound structure of the channel domain in the presence of a membrane potential (*75*−*77*).

ACKNOWLEDGMENT

We thank Professor Erwin London (State University of New York, Stony Brook, NY) for the gift of the 10-DN for use in the *Q* ratio measurements. We also thank Ms. Yun Liu (University of Guelph) for her aid in making the illustrations shown in panels A and B of Figure 5.

REFERENCES

1. Eraso, J. M., Chidambaram, M., and Weinstock, G. M. (1996) Increased production of colicin E1 in stationary phase, *J. Bacteriol. 178*, 1928−1935.
2. Kleanthous, C., and Walker, D. (2001) Immunity proteins: Enzyme inhibitors that avoid the active site, *Trends Biochem. Sci. 26*, 624−631.
3. Gould, J. M., and Cramer, W. A. (1977) Studies on the depolarization of the *Escherichia coli* cell membrane by colicin E1, *J. Biol. Chem. 252*, 5491−5497.
4. Masaki, H., and Ogawa, T. (2002) The modes of action of colicins E5 and D, and related cytotoxic tRNases, *Biochimie 84*, 433−438.

5. Harkness, R. E., and Braun, V. (1989) Colicin M inhibits peptidoglycan biosynthesis by interfering with lipid carrier recycling, *J. Biol. Chem. 264*, 6177−6182.
6. Cooper, P. C., and James, R. (1984) Two new E colicins, E8 and E9, produced by a strain of *Escherichia coli*, *J. Gen. Microbiol. 130*, 209−215.
7. Lazdunski, C. J., Bouveret, E., Rigal, A., Journet, L., Lloubes, R., and Benedetti, H. (1998) Colicin import into *Escherichia coli* cells, *J. Bacteriol. 180*, 4993−5002.
8. Lindeberg, M., Zakharov, S. D., and Cramer, W. A. (2000) Unfolding pathway of the colicin E1 channel protein on a membrane surface, *J. Mol. Biol. 295*, 679−692.
9. Berne, S., Sepcic, K., Anderluh, G., Turk, T., Macek, P., and Poklar, U. N. (2005) Effect of pH on the pore forming activity and conformational stability of ostreolysin, a lipid raft-binding protein from the edible mushroom *Pleurotus ostreatus*, *Biochemistry 44*, 11137−11147.
10. Ladokhin, A. S., Isas, J. M., Haigler, H. T., and White, S. H. (2002) Determining the membrane topology of proteins: Insertion pathway of a transmembrane helix of annexin 12, *Biochemistry 41*, 13617−13626.
11. Garcia-Saez, A. J., Mingarro, I., Perez-Paya, E., and Salgado, J. (2004) Membrane-insertion fragments of Bcl-xL, Bax, and Bid, *Biochemistry 43*, 10930−10943.
12. Schendel, S. L., Montal, M., and Reed, J. C. (1998) Bcl-2 family proteins as ion-channels, *Cell Death Differ. 5*, 372−380.
13. Filloux, A., Voulhoux, R., Ize, B., Gerard, F., Ball, G., and Wu, L. F. (2002) Use of colicin-based genetic tools for studying bacterial protein transport, *Biochimie 84*, 489−497.
14. Zakharov, S. D., Kotova, E. A., Antonenko, Y. N., and Cramer, W. A. (2004) On the role of lipid in colicin pore formation, *Biochim. Biophys. Acta 1666*, 239−249.
15. Brunden, K. R., Cramer, W. A., and Cohen, F. S. (1984) Purification of a small receptor-binding peptide from the central region of the colicin E1 molecule, *J. Biol. Chem. 259*, 190−196.
16. Taylor, R., Burgner, J. W., Clifton, J., and Cramer, W. A. (1998) Purification and characterization of monomeric *Escherichia coli* vitamin B12 receptor with high affinity for colicin E3, *J. Biol. Chem. 273*, 31113−31118.
17. Zakharov, S. D., and Cramer, W. A. (2004) On the mechanism and pathway of colicin import across the *E. coli* outer membrane, *Front Biosci. 9*, 1311−1317.
18. Tian, C., Tetreault, E., Huang, C. K., and Dahms, T. E. (2006) Electrostatic interactions of colicin E1 with the surface of *Escherichia coli* total lipid, *Biochim. Biophys. Acta 1758*, 693−701.
19. Shin, Y. K., Levinthal, C., Levinthal, F., and Hubbell, W. L. (1993) Colicin E1 binding to membranes: Time-resolved studies of spin-labeled mutants, *Science 259*, 960−963.
20. Kim, Y., Valentine, K., Opella, S. J., Schendel, S. L., and Cramer, W. A. (1998) Solid-state NMR studies of the membrane-bound closed state of the colicin E1 channel domain in lipid bilayers, *Protein Sci. 7*, 342−348.
21. Zakharov, S. D., Lindeberg, M., and Cramer, W. A. (1999) Kinetic description of structural changes linked to membrane import of the colicin E1 channel protein, *Biochemistry 38*, 11325−11332.
22. Dankert, J. R., Uratani, Y., Grabau, C., Cramer, W. A., and Hermodson, M. (1982) On a domain structure of colicin E1. A COOH-terminal peptide fragment active in membrane depolarization, *J. Biol. Chem. 257*, 3857−3863.
23. Elkins, P., Bunker, A., Cramer, W. A., and Stauffacher, C. V. (1997) A mechanism for toxin insertion into membranes is suggested by the crystal structure of the channel-forming domain of colicin E1, *Structure 5*, 443−458.
24. Parker, M. W., Postma, J. P., Pattus, F., Tucker, A. D., and Tsernoglou, D. (1992) Refined structure of the pore-forming domain of colicin A at 2.4 Å resolution, *J. Mol. Biol. 224*, 639−657.
25. Wiener, M., Freymann, D., Ghosh, P., and Stroud, R. M. (1997) Crystal structure of colicin Ia, *Nature 385*, 461−464.
26. Vetter, I. R., Parker, M. W., Tucker, A. D., Lakey, J. H., Pattus, F., and Tsernoglou, D. (1998) Crystal structure of a colicin N fragment suggests a model for toxicity, *Structure 6*, 863−874.
27. Hilsenbeck, J. L., Park, H., Chen, G., Youn, B., Postle, K., and Kang, C. (2004) Crystal structure of the cytotoxic bacterial protein colicin B at 2.5 Å resolution, *Mol. Microbiol. 51*, 711−720.
28. Song, H. Y., and Cramer, W. A. (1991) Membrane topography of ColE1 gene products: The immunity protein, *J. Bacteriol. 173*, 2935−2943.
29. Malenbaum, S. E., Merrill, A. R., and London, E. (1998) Membrane-inserted colicin E1 channel domain: A topological survey by fluorescence quenching suggests that model membrane thickness affects membrane penetration, *J. Nat. Toxins 7*, 269−290.
30. Petros, A. M., Nettesheim, D. G., Wang, Y., Olejniczak, E. T., Meadows, R. P., Mack, J., Swift, K., Matayoshi, E. D., Zhang, H., Thompson, C. B., and Fesik, S. W. (2000) Rationale for Bcl-xL/Bad peptide complex formation from structure, mutagenesis, and biophysical studies, *Protein Sci. 9*, 2528−2534.
31. Muchmore, S. W., Sattler, M., Liang, H., Meadows, R. P., Harlan, J. E., Yoon, H. S., Nettesheim, D., Chang, B. S., Thompson, C. B., Wong, S. L., Ng, S. L., and Fesik, S. W. (1996) X-ray and NMR structure of human Bcl-xL, an inhibitor of programmed cell death, *Nature 381*, 335−341.
32. Suzuki, M., Youle, R. J., and Tjandra, N. (2000) Structure of Bax: Coregulation of dimer formation and intracellular localization, *Cell 103*, 645−654.
33. McDonnell, J. M., Fushman, D., Milliman, C. L., Korsmeyer, S. J., and Cowburn, D. (1999) Solution structure of the proapoptotic molecule BID: A structural basis for apoptotic agonists and antagonists, *Cell 96*, 625−634.
34. Zakharov, S. D., Lindeberg, M., Griko, Y., Salamon, Z., Tollin, G., Prendergast, F. G., and Cramer, W. A. (1998) Membrane-bound state of the colicin E1 channel domain as an extended two-dimensional helical array, *Proc. Natl. Acad. Sci. U.S.A. 95*, 4282−4287.
35. Palmer, L. R., and Merrill, A. R. (1994) Mapping the membrane topology of the closed state of the colicin E1 channel, *J. Biol. Chem. 269*, 4187−4193.
36. Tory, M. C., and Merrill, A. R. (1999) Adventures in membrane protein topology. A study of the membrane-bound state of colicin E1, *J. Biol. Chem. 274*, 24539−24549.
37. Tory, M. C., and Merrill, A. R. (2002) Determination of membrane protein topology by red-edge excitation shift analysis: Application to the membrane-bound colicin E1 channel peptide, *Biochim. Biophys. Acta 1564*, 435−448.
38. Salwinski, L., and Hubbell, W. L. (1999) Structure in the channel forming domain of colicin E1 bound to membranes: The 402−424 sequence, *Protein Sci. 8*, 562−572.
39. Musse, A. A., Wang, J., Deleon, G. P., Prentice, G. A., London, E., and Merrill, A. R. (2006) Scanning the membrane-bound conformation of helix 1 in the colicin E1 channel domain by site-directed fluorescence labeling, *J. Biol. Chem. 281*, 885−895.
40. White, D., Musse, A. A., Wang, J., London, E., and Merrill, A. R. (2006) Toward elucidating the membrane topology of helix two of the colicin e1 channel domain, *J. Biol. Chem. 281*, 32375−32384.
41. Schendel, S. L., and Reed, J. C. (2000) Measuring pore formation by Bcl-2 family proteins, *Methods Enzymol. 322*, 274−282.
42. Musse, A. A., and Merrill, A. R. (2003) The molecular basis for the pH-activation mechanism in the channel-forming bacterial colicin E1, *J. Biol. Chem. 278*, 24491−24499.
43. Fraczkiewicz, R., and Braun, W. (1998) Exact and efficient analytical calculation of the accessible surface areas and their gradients for macromolecules, *J. Comput. Chem. 19*, 319−333.
44. Zhao, G., and London, E. (2005) Behavior of Diphtheria Toxin T Domain Containing Substitutions That Block Normal Membrane Insertion at Pro345 and Leu307: Control of Deep Membrane Insertion and Coupling between Deep Insertion of Hydrophobic Subdomains, *Biochemistry 44*, 4488−4498.
45. Cornette, J. L., Cease, K. B., Margalit, H., Spouge, J. L., Berzofsky, J. A., and DeLisi, C. (1987) Hydrophobicity scales and computational techniques for detecting amphipathic structures in proteins, *J. Mol. Biol. 195*, 659−685.
46. Merrill, A. R., Cohen, F. S., and Cramer, W. A. (1990) On the nature of the structural change of the colicin E1 channel peptide necessary for its translocation-competent state, *Biochemistry 29*, 5829−5836.
47. Huang, W., and Levitt, D. G. (1977) Theoretical calculation of the dielectric constant of a bilayer membrane, *Biophys. J. 17*, 111−128.
48. Raudino, A., and Mauzerall, D. (1986) Dielectric properties of the polar head group region of zwitterionic lipid bilayers, *Biophys. J. 50*, 441−449.
49. Lakowicz, J. R. (2006) *Principles of Fluorescence Spectroscopy*, Springer Science Media, New York, 2006.
50. Caputo, G. A., and London, E. (2003) Using a Novel Dual Fluorescence Quenching Assay for Measurement of Tryptophan

Depth within Lipid Bilayers To Determine Hydrophobic α-Helix Locations within Membranes, *Biochemistry 42*, 3265−3274.

51. Hayashibara, M., and London, E. (2005) Topography of diphtheria toxin A chain inserted into lipid vesicles, *Biochemistry 44*, 2183−2196.
52. Wang, J., Rosconi, M. P., and London, E. (2006) Topography of the hydrophilic helices of membrane-inserted diphtheria toxin T domain: TH1-TH3 as a hydrophilic tether, *Biochemistry 45*, 8124−8134.
53. Lakey, J. H., and Slatin, S. L. (2001) Pore-forming colicins and their relatives, *Curr. Top. Microbiol. Immunol. 257*, 131−161.
54. Jakes, K. S., Kienker, P. K., and Finkelstein, A. (1999) Channel-forming colicins: Translocation (and other deviant behaviour) associated with colicin Ia channel gating, *Q. Rev. Biophys. 32*, 189−205.
55. Stroud, R. M., Reiling, K., Wiener, M., and Freymann, D. (1998) Ion-channel-forming colicins, *Curr. Opin. Struct. Biol. 8*, 525−533.
56. Gouaux, E. (1997) The long and short of colicin action: The molecular basis for the biological activity of channel-forming colicins, *Structure 5*, 313−317.
57. Cramer, W. A., Heymann, J. B., Schendel, S. L., Deriy, B. N., Cohen, F. S., Elkins, P. A., and Stauffacher, C. V. (1995) Structure-function of the channel-forming colicins, *Annu. Rev. Biophys. Biomol. Struct. 24*, 611−641.
58. Slatin, S. L., Qiu, X. Q., Jakes, K. S., and Finkelstein, A. (1994) Identification of a translocated protein segment in a voltage-dependent channel, *Nature 371*, 158−161.
59. Wu, Z., Jakes, K. S., Samelson-Jones, B. S., Lai, B., Zhao, G., London, E., and Finkelstein, A. (2006) Protein translocation by bacterial toxin channels: A comparison of diphtheria toxin and colicin Ia, *Biophys. J. 91*, 3249−3256.
60. Gavel, Y., Nilsson, L., and von Heijne, G. (1988) Mitochondrial targeting sequences. Why 'non-amphiphilic' peptides may still be amphiphilic, *FEBS Lett. 235*, 173−177.
61. Monne, M., Nilsson, I., Johansson, M., Elmhed, N., and von Heijne, G. (1998) Positively and negatively charged residues have different effects on the position in the membrane of a model transmembrane helix, *J. Mol. Biol. 284*, 1177−1183.
62. Zhang, Y. L., and Cramer, W. A. (1992) Constraints imposed by protease accessibility on the trans-membrane and surface topography of the colicin E1 ion channel, *Protein Sci. 1*, 1666−1676.
63. Merrill, A. R., and Cramer, W. A. (1990) Identification of a voltage-responsive segment of the potential-gated colicin E1 ion channel, *Biochemistry 29*, 8529−8534.
64. Abrams, C. K., Jakes, K. S., Finkelstein, A., and Slatin, S. L. (1991) Identification of a translocated gating charge in a voltage-dependent channel. Colicin E1 channels in planar phospholipid bilayer membranes, *J. Gen. Physiol. 98*, 77−93.
65. Slatin, S. L., Duche, D., Kienker, P. K., and Baty, D. (2004) Gating movements of colicin A and colicin Ia are different, *J. Membr. Biol. 202*, 73−83.
66. Sobko, A. A., Kotova, E. A., Antonenko, Y. N., Zakharov, S. D., and Cramer, W. A. (2004) Effect of lipids with different spontaneous curvature on the channel activity of colicin E1: Evidence in favor of a toroidal pore, *FEBS Lett. 576*, 205−210.
67. Sobko, A. A., Kotova, E. A., Antonenko, Y. N., Zakharov, S. D., and Cramer, W. A. (2006) Lipid dependence of the channel properties of a colicin e1-lipid toroidal pore, *J. Biol. Chem. 281*, 14408−14416.
68. Anderluh, G., Dalla, S. M., Viero, G., Guella, G., Macek, P., and Menestrina, G. (2003) Pore formation by equinatoxin II, a eukaryotic protein toxin, occurs by induction of nonlamellar lipid structures, *J. Biol. Chem. 278*, 45216−45223.
69. Alvarez, C., Casallanovo, F., Shida, C. S., Nogueira, L. V., Martinez, D., Tejuca, M., Pazos, I. F., Lanio, M. E., Menestrina, G., Lissi, E., and Schreier, S. (2003) Binding of sea anemone pore-forming toxins sticholysins I and II to interfaces: Modulation of conformation and activity, and lipid-protein interaction, *Chem. Phys. Lipids 122*, 97−105.
70. Dempsey, C. E., Ueno, S., and Avison, M. B. (2003) Enhanced membrane permeabilization and antibacterial activity of a disulfide-dimerized magainin analogue, *Biochemistry 42*, 402−409.
71. Eun, S. Y., Jang, H. K., Han, S. K., Ryu, P. D., Lee, B. J., Han, K. H., and Kim, S. J. (2006) A helix-induced oligomeric transition of gaegurin 4, an antimicrobial peptide isolated from a Korean frog, *Mol. Cells 21*, 229−236.
72. Basanez, G., Sharpe, J. C., Galanis, J., Brandt, T. B., Hardwick, J. M., and Zimmerberg, J. (2002) Bax-type apoptotic proteins porate pure lipid bilayers through a mechanism sensitive to intrinsic monolayer curvature, *J. Biol. Chem. 277*, 49360−49365.
73. Yan, L., Miao, Q., Sun, Y., and Yang, F. (2003) tBid forms a pore in the liposome membrane, *FEBS Lett. 555*, 545−550.
74. Merrill, A. R., Steer, B. A., Prentice, G. A., Weller, M. J., and Szabo, A. G. (1997) Identification of a chameleon-like pH-sensitive segment within the colicin E1 channel domain that may serve as the pH-activated trigger for membrane bilayer association, *Biochemistry 36*, 6874−6884.
75. Horswell, S. L., Zamlynny, V., Li, H. Q., Merrill, A. R., and Lipkowski, J. (2002) Electrochemical and PM-IRRAS studies of potential controlled transformations of phospholipid layers on Au-(111) electrodes, *Faraday Discuss.*, 405−422.
76. Bin, X., Horswell, S. L., and Lipkowski, J. (2005) Electrochemical and PM-IRRAS studies of the effect of cholesterol on the structure of a DMPC bilayer supported at an Au (111) electrode surface, part 1: Properties of the acyl chains, *Biophys. J. 89*, 592−604.
77. Burgess, I., Li, M., Horswell, S. L., Szymanski, G., Lipkowski, J., Satija, S., and Majewski, J. (2005) Influence of the electric field on a bio-mimetic film supported on a gold electrode, *Colloids Surf., B 40*, 117−122.

BI700317K